

## RELIABILITY OF BLACK HOLE MASS ESTIMATION FROM BROAD EMISSION LINES IN SPECTRA OF THE TYPE 1 ACTIVE GALACTIC NUCLEI

Sladjana Marčeta-Mandić<sup>1,2</sup> 

<sup>1</sup>*Astronomical Observatory, Volgina 7, 11060 Belgrade, Serbia*

<sup>2</sup>*Department of Astronomy, Faculty of Mathematics, University of Belgrade  
Studentski trg 16, 11000 Belgrade, Serbia*

E-mail: [sladjana@aob.rs](mailto:sladjana@aob.rs)

(Received: October 9, 2024; Accepted: May 7, 2025)

**SUMMARY:** This study investigates reliability of the black hole mass ( $M_{\text{BH}}$ ) estimation using broad emission lines in spectra of the Type 1 Active Galactic Nuclei (AGN) from the Sloan Digital Sky Survey (SDSS). Masses derived from the broad  $\text{H}\alpha$  and  $\text{H}\beta$  emission lines are compared with the stellar velocity dispersion ( $\sigma_*$ ). The results show that the  $M_{\text{BH}}-\sigma_*$  correlation strengthens in spectral sub-samples characterized by broader  $\text{H}\beta$ , red asymmetry in  $\text{H}\beta$  profiles, high continuum luminosity, and absence of outflows. These findings suggest that  $\text{H}\alpha$  and  $\text{H}\beta$  provide more accurate black hole mass estimates for objects with such spectral properties.

**Key words.** Galaxies: active – quasars: supermassive black holes – quasars: emission lines

### 1. INTRODUCTION

An active galactic nucleus (AGN) is a compact region in the center of an active galaxy, with a luminosity up to  $10^4$  times higher than that of a typical galaxy. This luminosity excess originates from the gas accreting onto the supermassive black hole (SMBH) situated in the AGN core. The typical AGN structure can be described using the Unified Model (Antonucci 1993, Osterbrock and Ferland 2006): an SMBH, with mass in the range ( $10^6-10^{10}$ )  $M_{\odot}$  at the active galaxy center, is surrounded by a geometrically thin and optically thick accretion disc, extending outward into a vast dusty torus reaching scales of tens of parsecs (see, e.g., Osterbrock and Ferland 2006, Netzer 2013). Beyond the outer edges of the torus, further away from the AGN, lies the host

galaxy. Above and below the accretion disc there are regions filled with clumps of optically thick gas, which are accelerated by the SMBH's gravitational field to velocities ranging from a few thousand to tens of thousands of km/s (Peterson 2006). The continuum radiation emitted by the accretion disc ionizes the gas in these regions, producing numerous emission lines observed in the AGN spectra.

The gravitational field of SMBH highly influences the kinematics of the ionized gas, especially in the nearest region named the broad line region (BLR), where the broad emission lines (BELs) originate (see, e.g., Osterbrock and Ferland 2006, Netzer 2013). Hence, a highly ionized, fast-moving, BLR gas impacts the BELs parameters from which we can derive information on the SMBH mass (see, e.g., Sulentic et al. 2000, Peterson et al. 2004, Vestergaard and Peterson 2006, Peterson 2014). Additionally, some non-gravitational motion of the gas in BLR may be occurring due to the physical complexity of the site in the vicinity of SMBH and the accretion disc (see,

---

© 2025 The Author(s). Published by Astronomical Observatory of Belgrade and Faculty of Mathematics, University of Belgrade. This open access article is distributed under CC BY-NC-ND 4.0 International licence.

e.g., Popović et al. 2019, 2023a), which then affects the structure and kinematics of the BLR and BELs shapes, and, consequently, might impact the SMBH mass estimation ( $M_{\text{BH}}$ ).

As the BLR gas is predominantly moving in Keplerian orbits around SMBH (Osterbrock and Ferland 2006, Vestergaard and Peterson 2006, Gaskell 2009, Netzer 2013), the motion causes a broadening of emission lines from this region due to the Doppler effect. From the width of BELs, the velocity dispersion of the gas could be estimated. Assuming the virial relationship between the line width and distance of emitters from the central mass, the virial theorem could be used for the  $M_{\text{BH}}$  estimation (see Peterson et al. 2004, Peterson 2006, 2014), as shown in Eq. 1:

$$M_{\text{BH}} = f \left( \frac{R_{\text{BLR}} \Delta V^2}{G} \right), \quad (1)$$

where  $R_{\text{BLR}}$  is the distance of BLR from the central SMBH,  $G$  is the gravitational constant, and  $\Delta V$  is the velocity dispersion of the gas, usually determined from the Full Width at Half Maximum (FWHM) of BELs. The scaling factor  $f$  is a dimensionless parameter that accounts for the unknown geometry and orientation of BLR.

The most reliable method for a direct estimation of the BLR dimensions ( $R_{\text{BLR}}$ ) and its distance from the central source is reverberation mapping (RM) as introduced by Blandford and McKee (1982). The initial sample of AGNs with RM measurements revealed an empirical radius-luminosity ( $R - L$ ) relationship which enables the estimation of the BLR radius from continuum luminosity. This relationship allows for estimation the SMBH masses in AGNs from single-epoch observations (see, e.g., Peterson 2006, Shen 2013, Peterson 2014). As the sample of AGNs with the RM measurements has grown, some studies have shown that the  $R - L$  relation oversimplifies the dynamics and requires an additional parameter, the Eddington ratio (Dalla Bontà and Peterson 2022, Dalla Bontà et al. 2024). Therefore, several corrections for the  $R - L$  relation accounting for the Eddington ratio have been proposed (Grier et al. 2017, Du and Wang 2019, Dalla Bontà et al. 2020).

The most common single-epoch virial method for estimations of  $M_{\text{BH}}$  for low-redshift active galaxies uses the optical continuum luminosity at  $\lambda 5100 \text{ \AA}$  (the relationship is  $R_{\text{BLR}} - L_{5100}$ ) and the width of the broad  $\text{H}\beta$  emission line (Full Width at Half Maximum, further FWHM) (Vestergaard and Peterson 2006, Shen et al. 2015, Popović 2020).

Greene and Ho (2005) found that the broad  $\text{H}\alpha$  emission line can also be suitable for estimation of  $M_{\text{BH}}$ . This method relies on the empirical correlation between the scaled  $\text{H}\alpha$  luminosity and optical continuum luminosity at  $\lambda 5100 \text{ \AA}$ , and the strong correlation between the  $\text{H}\alpha$  and  $\text{H}\beta$  broad emission line widths (see in Greene and Ho 2005,

Section 4), which enables an  $M_{\text{BH}}$  estimation based only on observations of the broad  $\text{H}\alpha$  emission line (line luminosity and its width).

Another spectroscopic method  $M_{\text{BH}} - \sigma_*$ , relies on the correlation between SMBH mass and velocity dispersion of stars in the bulge of the host galaxy, annotated by  $\sigma_*$  (see, e.g., Gebhardt et al. 2000a,b, Ferrarese and Merritt 2000, Tremaine et al. 2002). Initially, this relation was observed for nearby quiescent galaxies, where it was found that  $\sigma_*$  is in a strong correlation with black hole masses estimated from stellar kinematics and gas dynamics (Gebhardt et al. 2000a,b, Ferrarese and Merritt 2000, Tremaine et al. 2002). The same correlation was also confirmed for active galaxies (Gebhardt et al. 2000b, Ferrarese et al. 2001, Onken et al. 2004, Grier et al. 2013, etc.). Using the assumption that AGNs follow the same  $M_{\text{BH}} - \sigma_*$  relation as the quiescent galaxies, this relation was used for scaling the virial formula for the  $M_{\text{BH}}$  estimation by calculating an average virial factor  $\langle f \rangle$  (see Woo et al. 2015, Batista et al. 2017, and references therein).

This method is completely independent of the virial method, which uses the kinematics of gas in the BLR (see, e.g., Greene and Ho 2005, Vestergaard and Peterson 2006, Harris et al. 2012, Shen et al. 2015). Therefore, it could be used to compare the SMBH masses estimated using the  $\text{H}\alpha$  and  $\text{H}\beta$  emission lines. Measuring the host galaxy stellar velocity dispersion of Type 1 AGNs is notoriously challenging, as the measurement of  $\sigma_*$  requires a high spatial resolution and thus is limited to relatively nearby galaxies. Additionally, the Type 1 AGNs luminosity excess complicates the observation of suitable stellar absorption lines within the black hole's radius of influence, which is requisite for  $\sigma_*$  measurements. Unfortunately, both these factors, in their respective ways, limit the number of Type 1 AGNs with reliable  $\sigma_*$  measurements. Consequently, the literature contains only limited references to such data.

In addition to the Keplerian motion of the BLR gas within the gravitational field of the SMBH, non-gravitational motions (such as outflows, flares, coronal winds, etc.) may arise in the regions where BELs originate. These motions, likely driven by the complex physical conditions in the vicinity of the SMBH and accretion disc, and often associated with matter accretion or relativistic jets (see, e.g., Popović et al. 2019, 2023a), introduce additional complexity to the structure and kinematics of BLR. Consequently, they can influence the shapes of BELs, potentially increasing broadening and asymmetry or producing multiple velocity components in the emission lines, which complicates their interpretation and may affect the estimation of the SMBH mass. For instance, the forbidden doublet  $[\text{O III}]\lambda\lambda 4959, 5007 \text{ \AA}$  was proven to be an effective tracer of gas outflows, commonly used to study ionized gas outflows in the narrow line region (NLR), and to investigate large-

scale gas outflows in AGNs (Woo et al. 2016, Kang et al. 2017, Kovačević-Dojčinović et al. 2022).

This study compares the SMBH masses derived using  $\sigma_*$  with those obtained via the virial method based on the broad emission lines  $H\alpha$  and  $H\beta$ . For this analysis, spectra from 90 Type 1 AGNs with publicly available and previously measured  $\sigma_*$  values were utilized (Harris et al. 2012, Shen et al. 2015, Bennert et al. 2015). The primary objective was to evaluate the reliability of the virial method when applied to different broad emission lines ( $H\alpha$  and  $H\beta$ ) and to investigate whether specific spectral line properties, emission line shapes, or features—including the presence or absence of gas outflows—can indicate which of these spectral lines are more reliable as the  $M_{\text{BH}}$  estimators.

Throughout this manuscript, the following cosmological parameters were used:  $H_0=70 \text{ km s}^{-1}\text{Mpc}^{-1}$ , and  $\Omega_\Lambda=0.7$  and  $\Omega_M=0.3$ .

The structure of this paper is as follows: Section 2 describes the sample selection as well as the decomposition and analysis of spectra. Section 3 presents the results, while Section 4 provides the discussion and conclusions.

## 2. SAMPLE AND ANALYSIS

For this research, we required well-documented Type 1 AGN objects that had a measured velocity dispersion of the stars in the host galaxy bulge. The sample was compiled from objects analyzed in studies by Harris et al. (2012) and Shen et al. (2015).

In their study, Harris et al. (2012) derived a spatially resolved stellar kinematics for a sample of 84 galaxies hosting Type 1 AGNs with redshifts between 0.02 and 0.09. This was accomplished by using long-slit spectra obtained from the 10 m W. M. Keck-1 Telescope. The  $\sigma_*$  profiles were measured across three distinct wavelength regions: Ca H&K, Mg Ib, and Ca II NIR. To determine  $\sigma_*$ , they employed a Python-based code that simultaneously fitted a linear combination of broadened stellar templates and a polynomial continuum to the data, using a Markov Chain Monte Carlo (MCMC) routine to identify the best-fit values.

The other group, as detailed by Shen et al. (2015), utilized high signal-to-noise ratio (SNR) co-added spectra from the Sloan Digital Sky Survey Reverberation Mapping (SDSS-RM) project. They employed the `vdispfit` routine (available in `idlSpec2d`) to measure  $\sigma_*$  from the host component of the decomposed galaxy spectra. Their study included a sample of 88 broad-line AGNs within the redshift range of  $0.1 < z < 1$ .

The spectra utilized in this research were sourced from the Sloan Digital Sky Survey (SDSS-III), Data Release 12<sup>1</sup> (DR12). The stellar velocity dispersions ( $\sigma_*$ ) were obtained from the works of Shen et al.

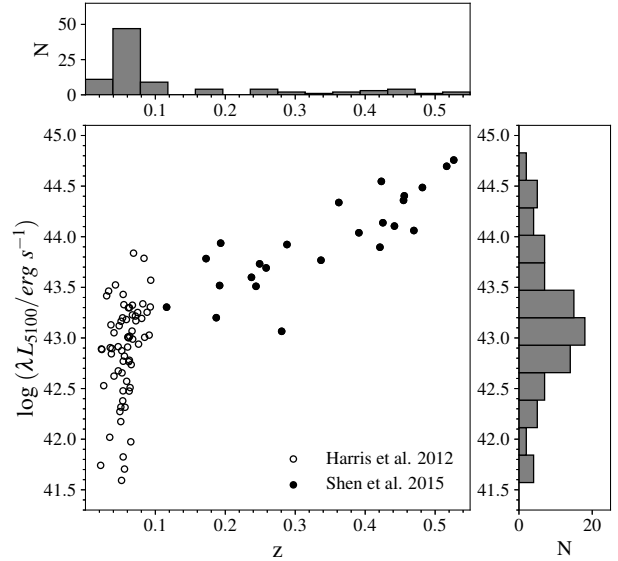


**Fig. 1:** The AGN luminosity (after subtracting the host galaxy contribution) as a function of redshift for the sample, along with their distributions.

(2015) and Harris et al. (2012). All objects with  $\sigma_* < 70 \text{ km s}^{-1}$  were excluded from the analysis, as this threshold corresponds to the limit of the SDSS instrumental resolution (Thomas et al. 2013). All objects with low SNR were removed from the sample, retaining primarily those with  $\text{SNR} > 20$ , which was necessary for performing complex fitting routines and analyzing line profiles meticulously. Additionally, the spectra examined in this study required the inclusion of  $H\alpha$  and  $H\beta$ , resulting in the exclusion of all objects lacking the  $H\alpha$  line due to their high cosmological redshift. As a result, the final sample contains 90 AGNs with redshifts in the range of  $0.02 < z < 0.53$ , including 24 from the Shen et al. (2015) sample and 66 from the Harris et al. (2012) sample (see Fig. 1).

The spectra were corrected for Galactic extinction using data from the NASA/IPAC Infrared Science Archive (IRSA)<sup>2</sup>, which provided extinction coefficients mapped along the line of sight by Schlegel et al. (1998). This correction was conducted under the assumption of a standard extinction law (as detailed in Howarth 1983). Subsequently, the spectra were adjusted for cosmological redshift.

The spectral principal component analysis (SPCA) was employed to eliminate the contributions from the host galaxy and retain the pure AGN emission for subsequent analysis (see Fig. 2). This method follows the procedures outlined in Vanden Berk et al. (2006), which involves non-parametric fitting of the observed spectra through a linear combination of 15 eigenspectra—ten corresponding to quasar eigenspectra and five representing galaxy

<sup>1</sup><https://www.sdss.org/dr12/>

<sup>2</sup><https://irsa.ipac.caltech.edu/applications/DUST/>

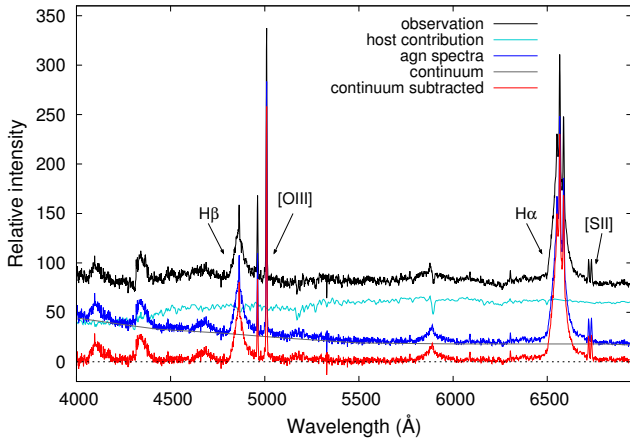


**Fig. 2:** An example of spectrum decomposition for object 1216-52709-0190 (SDSS plate-MJD-fiber) is shown, where the host galaxy and AGN contributions are separated using SPCA, followed by the continuum emission removal. The black line represents the observed spectrum, the green line shows the host galaxy contribution obtained from SPCA, and the blue line represents the AGN emission after subtracting the host galaxy component. The gray line corresponds to the continuum emission, while the red line shows the AGN spectrum after the continuum subtraction.

eigenspectra (see Yip et al. 2004a,b,c). A slight modification to the SPCA approach from Vanden Berk et al. (2006) involved masking all narrow emission lines in the host galaxy spectra derived from SPCA model and subtracting the modified host spectra from the observed spectra. This ensured that all narrow lines were preserved in the spectra utilized for further analysis. Finally, the continuum emission was removed from all spectra using the designated continuum windows (Kuraszkiewicz et al. 2002), as illustrated in Fig. 2. The measured continuum luminosity at  $\lambda 5100 \text{ \AA}$ , after removing the host galaxy contribution, is plotted against redshift (along with their distributions), is presented in Fig. 1 for the entire sample.

Spectra were finally fitted using a multi-Gaussian model for optical emission in the wavelengths ranges of  $\lambda\lambda 4000\text{--}5500 \text{ \AA}$  and  $\lambda\lambda 6200\text{--}6900 \text{ \AA}$ , as described by Kovačević et al. (2010) and Kovačević-Dojčinović and Popović (2015). When fitting the Balmer lines ( $H\alpha$  and  $H\beta$ ), it is common to employ three Gaussian functions for each line: one narrow line component representing the emission from the narrow line region (NLR), and two Gaussian components representing contributions from the broad line region (BLR). These are identified here as the very broad line component, which originates from the very broad line region (VBLR) near the supermassive black hole, and the intermediate line component, which arises from the intermediate line region (ILR) at a greater distance from the SMBH (see Popović et al. 2004, Bon

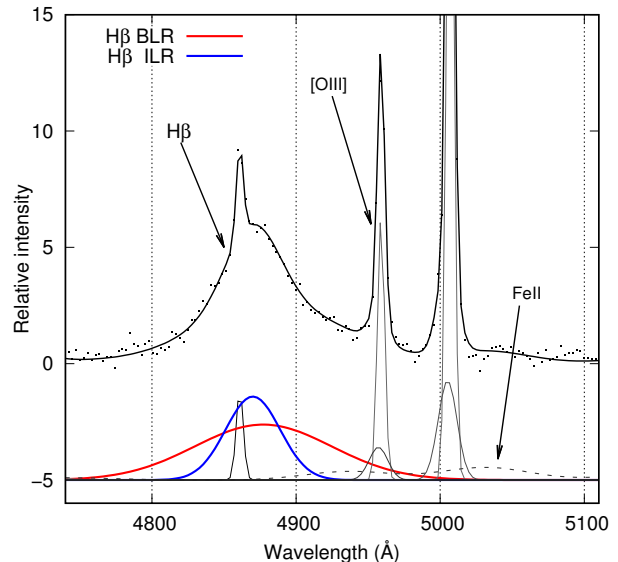
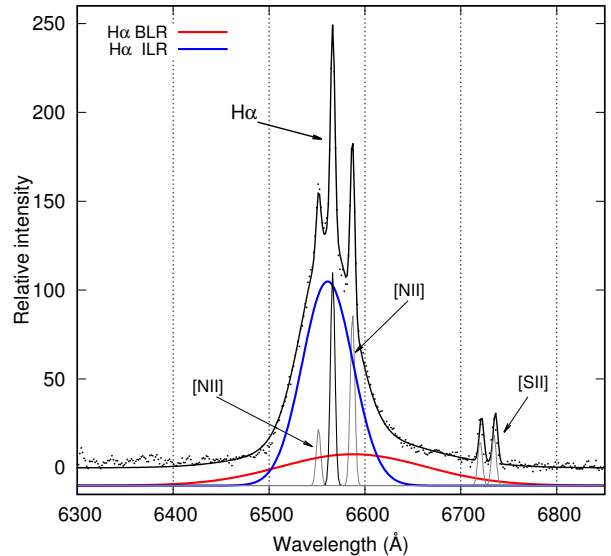


**Fig. 3:** Examples of decomposition of the  $H\alpha$  (top panel) and  $H\beta$  (bottom panel) emission lines for the object 0439-51877-0566 (SDSS plate-MJD-fiber). Both lines are modeled using one narrow and two broad Gaussian components. The observational data are shown as dots, the overall model as a solid line, and the optical FeII template as a dashed line. Narrow emission-line components are represented by thin lines, while broad components are shown as thick, solid-colored lines.

et al. 2006, Kovačević et al. 2010, etc). The broad emission lines of AGNs are often highly intricate and convoluted, reflecting the complexity of the BLR. As a result, a single Gaussian model is insufficient to accurately represent the emission from the BLR. Instead, a double-Gaussian model (VBLR+ILR) has been employed to characterize the shapes of these broad lines (see, e.g., Mullaney et al. 2013, Sexton et al. 2021).

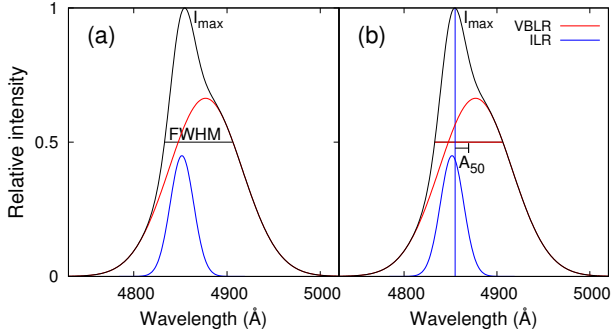


**Fig. 4:** An example of measurement of FWHM (*panel a*) and line asymmetry  $A_{50}$  (*panel b*) for the broad-line components (VBLR + ILR), with each component represented by a different solid-colored line.

The limitations of this two-component model approach arise from the uncertainty regarding the contributions of the ILR and VBLR Gaussians to the overall broad Balmer line profiles. Nonetheless, the model effectively describes various shapes of broad Balmer line profiles, even in cases where the spectra exhibit Lorentzian-like characteristics. These profiles can be accurately fitted using the ILR Gaussian at the line core, and the broader VBLR Gaussian in the wings of the line, where the ILR Gaussian is significantly more intense than the VBLR Gaussian.

The numerous FeII lines within the 4000 – 5500 Å range, which overlap with the broad H $\beta$  lines, were fitted using a semi-empirical iron template presented in Kovačević et al. (2010), along with additional lines as detailed in Shapovalova et al. (2012). Since the narrow [O III]  $\lambda\lambda$  4959, 5007 Å lines could have complex line profiles, they were fitted with a double-Gaussian model, where one Gaussian addresses the core and the other the wings of the lines (see Woo et al. 2016, Kovačević-Dojčinović et al. 2022). Both, the [O III]  $\lambda$ 4959 Å and [O III]  $\lambda$ 5007 Å lines, exhibit identical line profiles with their intensity ratio established at 2.99 (see Dimitrijević et al. 2007). The Gaussians fitted to the cores of the [O III]  $\lambda\lambda$  4959, 5007 Å lines are assumed to share the same width and shift as those fitted to the narrow Balmer lines. This assumption is based on the premise that all narrow lines originate from the same region (NLR), leading us to expect that these lines will exhibit similar shifts and widths. However, the wing components of the [O III]  $\lambda\lambda$  4959, 5007 Å doublet were modeled independently from other lines, allowing for free width and shift parameters (as shown in Kovačević et al. 2010). The [N II]  $\lambda\lambda$  6548, 6583 Å lines, which overlap with the broad H $\alpha$  line, are fitted with a single Gaussian for each line, sharing the same width and shift as the narrow H $\alpha$  component, with their intensity ratio set at 3.05 (Dojčinović et al. 2023).

An illustration of the decomposition of optical emission for H $\alpha$  and H $\beta$  is presented in Fig. 3. In this figure, the BEL profile is represented as the

sum of two broad Gaussians for both H $\alpha$  and H $\beta$ . The Full Width at Half Maximum (FWHM) and the asymmetry ( $A_{50}$ ) of BEL are measured as depicted in Fig. 4.  $A_{50}$  is defined as the difference between the centroid shift and the peak of the broad component at 50% of  $I_{max}$  (see Jonić et al. 2016).

### 3. RESULTS

The SMBH masses were estimated using FWHM of the broad H $\beta$  line and the continuum luminosity at 5100Å, applying the virial formula for  $M_{BH}$  from Vestergaard and Peterson (2006). For the estimation of the SMBH masses based on H $\alpha$ , FWHM of the broad H $\alpha$  line, and the luminosity of the H $\alpha$  line were used, following the formula provided by Greene and Ho (2005).

Firstly, the correlations between  $\sigma_*$  and the widths of the H $\alpha$  and H $\beta$  lines are compared and shown in Fig. 5. Then, the SMBH masses derived from H $\alpha$  and H $\beta$  were separately compared with the stellar velocity dispersions of the objects, relying on the well-established  $M_{BH} - \sigma_*$  relation. Additionally, the masses obtained from H $\alpha$  and H $\beta$  were directly compared.

For the full sample of 90 objects, the SMBH masses estimated using H $\alpha$  exhibited a stronger correlation with  $\sigma_*$  (Spearman correlation coefficient  $\rho = 0.41$ ,  $P_0 = 7 \times 10^{-5}$ ) compared to those derived from H $\beta$  and  $L_{5100}$  ( $\rho = 0.28$ ,  $P_0 = 9 \times 10^{-3}$ ), as shown in panels (a) and (b) of Fig. 6 or Fig. 7, under ‘total sample’ data. Furthermore, the comparison of the SMBH masses obtained via virial formulas from H $\alpha$  and H $\beta$  demonstrated a highly significant correlation ( $\rho = 0.81$ ,  $P_0 = 2 \times 10^{-22}$ ), as seen in panels (c) of Fig. 6 or Fig. 7, also under ‘total sample’ data.

The primary objective of this study was to investigate whether specific spectral characteristics of AGNs within the analyzed sample indicate physical or kinematic conditions in BLR that could enhance the correlation between the virial SMBH masses estimated from broad H $\alpha$  and H $\beta$  lines, and stellar velocity dispersions. Identifying such a sub-sample could suggest that AGNs with these spectral properties serve as more reliable  $M_{BH}$  estimators. Additionally, this investigation aims to highlight spectral features and their threshold values that characterize objects for which the virial formula provides less reliable  $M_{BH}$  estimates.

Several spectral characteristics were used to define sub-samples and evaluate the aforementioned correlations. The threshold values for each criterion were chosen to divide the sample into two equal-sized sub-samples for comparability. The criteria were:

- i) FWHM of H $\beta$  smaller/larger than 4500 km s $^{-1}$ ,
- ii) Asymmetry of the H $\beta$  profile ( $A_{50}$ ) smaller/larger than 30 km s $^{-1}$ ,
- iii) Continuum luminosity at  $\lambda$  5100 Å smaller/larger than  $1.5 \times 10^{43}$  erg s $^{-1}$ ,

- iv) Difference between  $\sigma_{[OIII]}$  and  $\sigma_*$  (a measure of outflow contribution in [O III] lines) smaller/larger than  $30 \text{ km s}^{-1}$ .

For each sub-sampling criterion, the correlations between  $\sigma_*$  and  $M_{\text{BH}}$  derived from  $H\alpha$  and  $H\beta$  were analyzed and are presented in Fig. 6 and Fig. 7. Panels (a) of these figures show correlations between  $\sigma_*$  and  $M_{\text{BH}}$  obtained using the  $H\alpha$  parameters, while panels (b) present correlations with  $M_{\text{BH}}$  estimated using  $H\beta$  and  $L_{5100}$ . Comparisons of the SMBH masses derived from  $H\alpha$  and  $H\beta$  are shown in panels (c). The Spearman correlation coefficients ( $\rho$ ) and the corresponding P-values are provided for the total sample (90 objects) and the different sub-samples.

### 3.1. Width of broad $H\beta$ line

The full width at half maximum (FWHM) of the  $H\beta$  line is a well-established indicator of gas velocity in BLR and, consequently, of the gravitational field strength in regions where the broad emission lines originate (Osterbrock and Ferland 2006, Vestergaard and Peterson 2006, Shen 2013, etc.). A comparison of correlation between  $\sigma_*$  and the  $H\alpha$  and  $H\beta$  line widths is shown in Fig. 5. For the analyzed sample,  $\sigma_*$  exhibits a stronger correlation with FWHM of the  $H\alpha$  emission line ( $\rho = 0.37$ ,  $P_0 = 10^{-4}$ ) compared to FWHM of the  $H\beta$  line ( $\rho = 0.27$ ,  $P_0 = 10^{-2}$ ).

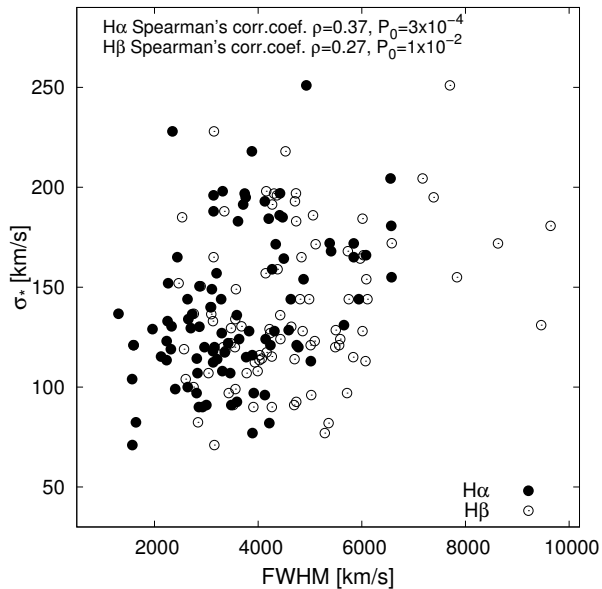


**Fig. 5:** Correlations between  $\sigma_*$  and  $\text{FWHM}_{H\alpha}$  (filled circle markers) and between  $\sigma_*$  and  $\text{FWHM}_{H\beta}$  (empty circle markers).

The sample division based on  $\text{FWHM}_{H\beta}$  at the threshold of  $4500 \text{ km s}^{-1}$  follows the established classification of AGNs into Populations A and B, where the conventional boundary is set at  $4000 \text{ km s}^{-1}$  (Sulentic et al. 2000, Marziani et al. 2001, Shen and Ho 2014). A slight adjustment in this study was made to ensure two sub-samples

of comparable sizes. Based on this criterion, the sample was divided into two sub-samples: 42 objects with broad  $H\beta$  ( $\text{FWHM}_{H\beta} > 4500 \text{ km s}^{-1}$ ) and 48 objects with narrower broad  $H\beta$  ( $\text{FWHM}_{H\beta} < 4500 \text{ km s}^{-1}$ ). The correlation between  $\sigma_*$  and  $M_{\text{BH}}$  derived from the  $H\alpha$  line parameters is only slightly stronger in the sub-sample with broader  $H\beta$  lines (see Fig. 6, panel a1). However, the correlation between  $\sigma_*$  and  $M_{\text{BH}}$  estimated using  $H\beta$  and  $L_{5100}$  is significantly stronger in the sub-sample with broader  $H\beta$  lines (see Fig. 6, panel b1). In contrast, no correlation is observed for objects with narrower broad  $H\beta$  lines ( $\text{FWHM}_{H\beta} < 4500 \text{ km s}^{-1}$ ). A comparison of the SMBH masses derived from the  $H\alpha$  and  $H\beta$  line parameters reveals a substantially stronger correlation for objects with broader  $H\beta$  ( $\rho = 0.88$ ,  $P_0 = 10^{-14}$ ) than for the sub-sample with narrower broad  $H\beta$  lines ( $\rho = 0.68$ ,  $P_0 = 10^{-7}$ ). These correlations are illustrated in Fig. 6, panel (c1).

Applying the sample division based on a  $\text{FWHM}_{H\beta}$  threshold of  $4000 \text{ km s}^{-1}$  does not significantly change the results, although the sub-sample with  $\text{FWHM}_{H\beta} > 4000 \text{ km s}^{-1}$  contains more objects (58), while the sub-sample with  $\text{FWHM}_{H\beta} < 4000 \text{ km s}^{-1}$  contains only 32. For objects with  $\text{FWHM}_{H\beta} > 4000 \text{ km s}^{-1}$ , the correlation between the SMBH masses estimated using  $H\beta$  and  $L_{5100}$  is slightly weaker ( $\rho = 0.24$ ,  $P_0 = 7 \times 10^{-2}$ ) compared to the correlation for the sub-sample with  $\text{FWHM}_{H\beta} > 4500 \text{ km s}^{-1}$ , while no correlation is found for the sub-sample with  $\text{FWHM}_{H\beta} < 4000 \text{ km s}^{-1}$ . For masses obtained from  $H\alpha$ , adjusting the threshold has no impact on the correlation between  $\sigma_*$  and  $M_{\text{BH}}$ .

### 3.2. Asymmetry of broad $H\beta$ line profiles

The blue asymmetry of the broad  $H\beta$  line ( $A_{50}$ ) is generally interpreted as evidence of directed gas motion, possibly non-virial, toward the observer (such as outflows, flares, coronal winds, etc.) (Jonić et al. 2016, Popović et al. 2019). In contrast to the blue asymmetry, the red asymmetry observed in broad emission lines is a more complex phenomenon. It may arise from the inflow of radiating gas or reflect the gravitational influence of SMBH, serving as an indicator of the strength of its gravitational field as first proposed by Netzer (1977). In this interpretation, the redward asymmetry results from gravitational redshift caused by the strong gravitational influence of SMBH, implying that a part of the emitting gas is located very close to it where the relativistic effects become significant. Numerous studies have explored this phenomenon in detail (see, e.g., Zheng and Sulentic 1990, Popović et al. 1995, Bon et al. 2015, Jonić et al. 2016, Mediavilla et al. 2018, Popović et al. 2019, Punsly et al. 2020, Mediavilla and Jiménez-Vicente 2021, Marziani 2023, etc.), suggesting that the gravitational redshift could play an important role in producing the red asymmetry in broad emission line profiles.

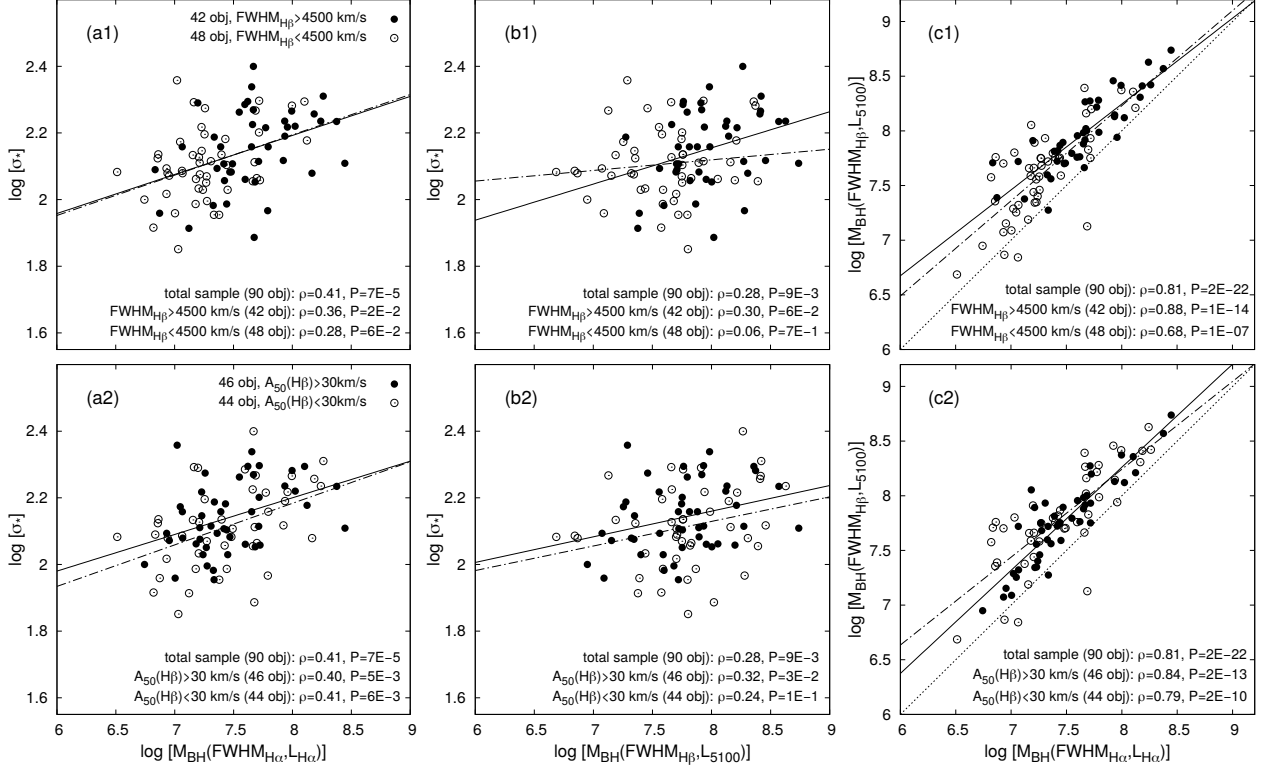


**Fig. 6:** Correlations between  $\sigma_*$  and  $M_{\text{BH}}$ , estimated using the  $\text{H}\alpha$  and  $\text{H}\beta$  line parameters, for the total sample and various sub-samples. Sub-samples are defined based on  $\text{FWHM}_{\text{H}\beta}$  (panels a1, b1, and c1) and  $\text{H}\beta$  asymmetry ( $A_{50}$ ) (panels a2, b2, and c2). For the sub-sample with  $\text{FWHM}_{\text{H}\beta} < 4500 \text{ km s}^{-1}$ , the best linear fit is shown as the dash-dotted line (empty circle markers), while for  $\text{FWHM}_{\text{H}\beta} > 4500 \text{ km s}^{-1}$ , it is represented by the solid line (filled circle markers) in panels a1, b1, and c1. In panel c1, the dotted line indicates the one-to-one relation. The same notation applies to sub-samples defined by  $A_{50}$ , with a threshold of  $30 \text{ km s}^{-1}$ , in panels a2, b2, and c2.

The sample is divided into two sub-samples: one consisting of objects with a significant red asymmetry in the broad  $\text{H}\beta$  profile and the other containing objects with either no significant asymmetry (weak asymmetry) or with a blue asymmetry. Given that the SDSS instrumental resolution limit for spectra is  $70 \text{ km s}^{-1}$  (Thomas et al. 2013), the threshold for sample division was set to a value greater than zero to ensure a more reliable classification based on this criterion. The threshold was set at  $30 \text{ km s}^{-1}$  to obtain two sub-samples of comparable sizes. Thus, with the threshold at  $30 \text{ km s}^{-1}$ , two sub-samples were formed: the first sub-sample ( $A_{50} < 30 \text{ km s}^{-1}$ ) consists of 46 objects exhibiting either a blue asymmetry or no significant asymmetry, while the second sub-sample ( $A_{50} > 30 \text{ km s}^{-1}$ ) includes 44 objects with a significant red asymmetry in the  $\text{H}\beta$  profile.

The presence of a red or blue asymmetry in the broad  $\text{H}\beta$  line does not affect the correlation between  $\sigma_*$  and  $M_{\text{BH}}$  when masses are estimated using the  $\text{H}\alpha$  line (see Fig. 6, panel a2). However, for masses estimated using  $\text{H}\beta$  and  $L_{5100}$ , the correlation between  $\sigma_*$  and  $M_{\text{BH}}$  is slightly stronger for objects

with a red asymmetry in  $\text{H}\beta$  ( $A_{50} > 30 \text{ km s}^{-1}$ ), with  $\rho = 0.32$  and  $P_0 = 3 \times 10^{-2}$ , compared to those with no strong asymmetry or with a blue asymmetry ( $A_{50} < 30 \text{ km s}^{-1}$ ), where the correlation is weaker ( $\rho = 0.24$ ,  $P_0 = 10^{-1}$ ), as shown in Fig. 6, panel (b2).

When comparing the SMBH masses estimated using  $\text{H}\alpha$  and  $\text{H}\beta$ , the correlation is slightly stronger for objects exhibiting red asymmetry in the  $\text{H}\beta$  line ( $A_{50} > 30 \text{ km s}^{-1}$ ), with Spearman correlation coefficient of  $\rho = 0.84$  and  $P_0 = 10^{-13}$ , than for objects with no strong asymmetry or with a blue asymmetry in  $\text{H}\beta$  ( $A_{50} < 30 \text{ km s}^{-1}$ ), for which  $\rho = 0.79$  and  $P_0 = 10^{-10}$  (see Fig. 6, panel c2).

Applying a stricter sample division at an  $A_{50}$  threshold of  $70 \text{ km s}^{-1}$  (instrumental resolution) makes some correlations more pronounced. With this criterion, the sub-sample with  $A_{50} > 70 \text{ km s}^{-1}$  contains 35 objects, while the sub-sample with  $A_{50} < 70 \text{ km s}^{-1}$  contains 55 objects. The correlation between  $\sigma_*$  and  $M_{\text{BH}}$  estimated using the  $\text{H}\alpha$  line improves slightly for the sub-sample with  $A_{50} > 70 \text{ km s}^{-1}$  ( $\rho = 0.46$ ,  $P_0 = 5 \times 10^{-3}$ ) compared to the sub-sample with  $A_{50} > 30 \text{ km s}^{-1}$ . Similarly, the correlation between  $\sigma_*$  and  $M_{\text{BH}}$  estimated using  $\text{H}\beta$

and  $L_{5100}$  is slightly stronger for the sub-sample with  $A_{50} > 70 \text{ km s}^{-1}$  ( $\rho = 0.37, P_0 = 3 \times 10^{-2}$ ) than for the sub-sample with  $A_{50} > 30 \text{ km s}^{-1}$ . However, adjusting the threshold does not affect the correlation between SMBH masses estimated from  $H\alpha$  and  $H\beta$ .

### 3.3. The continuum luminosity at $\lambda 5100 \text{ \AA}$

The continuum luminosity at  $\lambda 5100 \text{ \AA}$  is strongly correlated with the size of the broad-line region ( $R_{\text{BLR}}$ ), following the well-established  $R_{\text{BLR}} - L_{5100}$  relation (Kaspi et al. 2000, 2005, Bentz et al. 2006). Additionally, an excess in optical continuum luminosity is often attributed to emission from the accretion disc surrounding SMBH. More massive SMBHs generally exhibit a stronger optical emission, either due to higher accretion rates or the presence of more massive accretion discs (Ferrarese and Ford 2005, Shen 2013).

To investigate the role of luminosity, the sample was divided using a threshold of  $L_{5100} = 1.5 \times 10^{43} \text{ erg s}^{-1}$ . This resulted in two sub-samples: 47 objects with continuum luminosity below this limit and 43 objects with higher luminosity.

The correlation between  $\sigma_*$  and  $M_{\text{BH}}$  obtained from the broad  $H\alpha$  line parameters is stronger for the high-luminosity sub-sample ( $\rho = 0.52, P_0 = 3 \times 10^{-4}$ ) than for the low-luminosity sub-sample ( $\rho = 0.41, P_0 = 5 \times 10^{-3}$ ). A similar trend is observed for the  $M_{\text{BH}}$  estimates based on the  $H\beta$  line, where the correlation with  $\sigma_*$  is more pronounced in the high-luminosity subset ( $\rho = 0.43, P_0 = 4 \times 10^{-3}$ ), compared to the low-luminosity sub-sample,  $\rho = 0.30, P_0 = 4 \times 10^{-2}$  (see Fig. 7, panels a3 and b3).

Furthermore, the correlation between the SMBH masses derived from the  $H\alpha$  and  $H\beta$  line parameters is stronger in the high-luminosity sub-sample ( $\rho = 0.83, P_0 = 6 \times 10^{-12}$ ) compared to the low-luminosity sub-sample ( $\rho = 0.76, P_0 = 5 \times 10^{-10}$ ), as shown in Fig. 7, panel (c3).

### 3.4. Emission contribution from outflows

The profile of the [O III]  $\lambda\lambda 4959, 5007 \text{ \AA}$  emission line doublet is commonly used as an indicator of outflow emission (Rakshit and Woo 2018, Kovačević-Dojčinović et al. 2022). The [O III] emission originates in the narrow line region (NLR), located on kiloparsec scales, much farther from SMBH than BLR. The width of the [O III] lines is primarily influenced by virial motion associated with the host galaxy's gravitational potential, along with the non-virial ionized gas kinematics such as outflows (see, e.g., Bae et al. 2017, Kang and Woo 2018, Sexton et al. 2021). If the [O III] emission originates purely from gas in virial motion, the [O III] line widths should be comparable to the stellar velocity dispersion,  $\sigma_*$ . On the other hand, any discrepancy between  $\sigma_{[\text{O III}]}$  and  $\sigma_*$  may indicate the presence of non-virial gas motions, such as outflows driven by the AGN activity. In such cases, the contribution

of gas outflows can be estimated from the difference between  $\sigma_*$  and  $\sigma_{[\text{O III}]}$  (Woo et al. 2016, Rakshit and Woo 2018, Woo et al. 2020).

However, while the [O III] emission line is a valuable tracer of outflows in NLR, it does not necessarily reflect an outflow activity in BLR, nor does the detection of outflow signatures in the [O III] line profile imply the corresponding features in the broad Balmer line profiles. Studies, such as Zamanov et al. (2002) and Vietri et al. (2018), emphasize that different outflow mechanisms may operate in these regions, and that the NLR and BLR outflows can have distinct kinematic characteristics and driving forces. Nevertheless, these studies support the possibility that the outflows detected in the [O III] emission lines may be part of a larger, more complex outflow structure that extends from the BLR to the NLR, and potentially even farther. With these considerations in mind, we use the comparison between  $\sigma_{[\text{O III}]}$  and  $\sigma_*$  as a tracer of outflows.

Using a threshold of  $\sigma_{[\text{O III}]} - \sigma_* = 30 \text{ km s}^{-1}$  to divide the sample based on outflow contribution, we obtained two sub-samples:

- 47 objects with significant outflow contributions ( $\sigma_{[\text{O III}]} - \sigma_* > 30 \text{ km s}^{-1}$ ).
- 43 objects where outflow contributions are negligible ( $\sigma_{[\text{O III}]} - \sigma_* < 30 \text{ km s}^{-1}$ ).

The threshold was chosen arbitrarily to ensure two sub-samples of comparable sizes.

The sub-sample with negligible outflow contribution in narrow emission lines ( $\sigma_{[\text{O III}]} - \sigma_* < 30 \text{ km s}^{-1}$ ) exhibits a significantly stronger correlation between  $\sigma_*$  and  $M_{\text{BH}}$  estimated from the  $H\beta$  line ( $\rho = 0.47, P_0 = 10^{-3}$ ) compared to the sub-sample with a stronger outflow influence ( $\sigma_{[\text{O III}]} - \sigma_* > 30 \text{ km s}^{-1}$ ) where the correlation is weaker ( $\rho = 0.27, P_0 = 7 \times 10^{-2}$ , see Fig. 7, panel b4). On the other hand, no significant difference is found between these two sub-samples when comparing the correlation between  $\sigma_*$  and  $M_{\text{BH}}$  obtained using  $H\alpha$  (see Fig. 7, panel a4).

Additionally, the sub-sample with negligible outflow contribution shows a stronger correlation between the SMBH masses estimated from  $H\alpha$  and  $H\beta$  ( $\rho = 0.87, P_0 = 10^{-14}$ ) compared to the sub-sample with prominent outflow contributions ( $\rho = 0.79, P_0 = 10^{-11}$ ), as shown in Fig. 7, panel (c4).

### 3.5. Influence of the $R - L$ scaling law on the $M_{\text{BH}}$ estimation

The influence of different  $R - L$  scaling laws on single-epoch  $M_{\text{BH}}$  estimates is examined using the formulas for the  $M_{\text{BH}}$  calculation provided by Dalla Bontà et al. (2020) for  $M_{\text{BH}}(H\beta)$  and by Dalla Bontà et al. (2024) for  $M_{\text{BH}}(H\alpha)$ . These formulas incorporate a more recent scaling law that accounts for the Eddington ratio. The results are compared

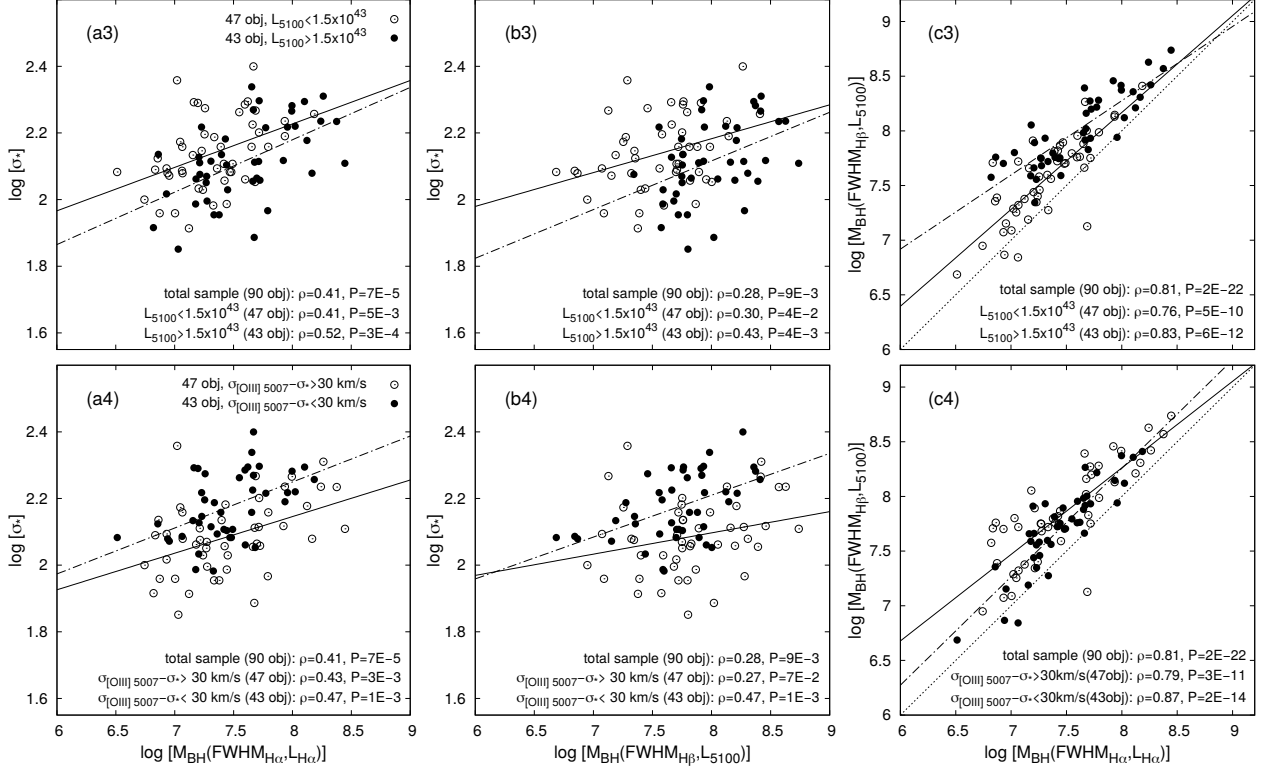


**Fig. 7:** Same as Fig. 6, but for sub-samples divided by  $L_{5100} = 1.5 \times 10^{43} \text{ erg s}^{-1}$  (panels a3, b3, c3) and by  $\sigma_{[OIII]} - \sigma_* = 30 \text{ km s}^{-1}$  (panels a4, b4, c4).

with the previously calculated  $M_{\text{BH}}$  values obtained using the formulas from [Greene and Ho \(2005\)](#) for  $M_{\text{BH}}(\text{H}\alpha)$  and [Vestergaard and Peterson \(2006\)](#) for  $M_{\text{BH}}(\text{H}\beta)$ .

The comparison reveals that for both lines, the  $M_{\text{BH}}$  values obtained using the updated scaling law strongly correlate with the previous  $M_{\text{BH}}$  estimates ( $\rho \approx 0.94$ ,  $P_0 = 0$ ). Additionally, it is found that accounting for the Eddington ratio in the  $R - L$  scaling law systematically lowers the estimated SMBH masses, which is consistent with similar findings reported by [Dalla Bontà et al. \(2024\)](#).

The black hole masses obtained using [Dalla Bontà et al. \(2020, 2024\)](#) are further compared with the stellar velocity dispersion. The correlation coefficient between  $\sigma_*$  and  $M_{\text{BH}}(\text{H}\alpha)$  calculated using [Dalla Bontà et al. \(2024\)](#) is slightly weaker ( $\rho = 0.36$ ,  $P_0 < 10^{-4}$ ) compared to the estimates obtained using [Greene and Ho \(2005\)](#) for the total sample (see Fig. 6 and 7). A similar trend is observed for the correlation between  $\sigma_*$  and  $M_{\text{BH}}(\text{H}\beta)$ , where the  $M_{\text{BH}}$  values estimated using [Dalla Bontà et al. \(2020\)](#) yield a slightly lower correlation coefficient ( $\rho = 0.21$ ,  $P_0 < 10^{-2}$ ) compared to those estimated using [Vestergaard and Peterson \(2006\)](#).

Nevertheless, the correlation between the black hole masses derived from the  $\text{H}\alpha$  and  $\text{H}\beta$  lines is slightly stronger when using the updated  $R - L$  scaling law ( $\rho = 0.89$ ,  $P_0 = 0$ ) compared to

the correlation between  $M_{\text{BH}}(\text{H}\alpha)$  and  $M_{\text{BH}}(\text{H}\beta)$  obtained with the formulas from [Greene and Ho \(2005\)](#) and [Vestergaard and Peterson \(2006\)](#).

#### 4. DISCUSSION AND CONCLUSIONS

This study investigated the reliability of the SMBH mass ( $M_{\text{BH}}$ ) estimates based on Balmer BELs in Type 1 AGN spectra by comparing  $M_{\text{BH}}$  derived from the kinematic parameters of  $\text{H}\alpha$  and  $\text{H}\beta$  with stellar velocity dispersion,  $\sigma_*$ . The results indicate that the correlation between the SMBH masses estimated using either of these BELs and  $\sigma_*$  depends on specific spectral properties. The correlations are more significant for sub-samples of objects characterized by:

- Broader  $\text{H}\beta$  emission line profiles,
- Higher continuum luminosity at  $\lambda 5100 \text{ \AA}$ ,
- Red asymmetry in the  $\text{H}\beta$  line profile,
- Negligible outflow contributions to emission lines.

When comparing  $\text{H}\alpha$  and  $\text{H}\beta$  as the SMBH mass estimators, the analysis of the total sample suggests that masses estimated using  $\text{H}\alpha$  exhibit a somewhat stronger correlation with  $\sigma_*$  than those derived from  $\text{H}\beta$  and  $L_{5100}$ . This discrepancy may stem from uncertainties in fitting the  $\text{H}\beta$  profile due to its overlap with  $[\text{OIII}]$  and numerous  $\text{FeII}$  lines. Similarly, the  $L_{5100}$  measurements may be

affected by uncertainties in subtracting the host galaxy contribution. In extreme cases, where the Fe II emission is exceptionally broad and strong,  $L_{5100}$  can also be contaminated by the Fe II pseudo-continuum (Popović et al. 2023b), making it difficult to isolate the actual continuum emission.

The stronger correlation between  $\sigma_*$  and  $M_{\text{BH}}$  for objects with red asymmetry in  $\text{H}\beta$ , compared to those with blue asymmetry suggests that the blue asymmetry likely arises from a non-virialized gas motion directed toward the observer. This introduces an arbitrary contribution to the line profile, affecting FWHM of  $\text{H}\beta$  and, consequently, the SMBH mass estimation, making these objects less reliable for the  $M_{\text{BH}}$  determination. In contrast, the red asymmetry is likely a signature of gravitational redshift, implying that these profiles are not influenced by non-virial motion (see Jonić et al. 2016, Popović et al. 2019).

Previous studies by Jonić et al. (2016) and Popović et al. (2019) examined the profiles of broad  $\text{H}\beta$  and  $\text{MgII}$  lines and concluded that the blue asymmetries in these profiles likely indicate the presence of a non-virialized motion. Thus, these lines should be used with caution when estimating  $M_{\text{BH}}$ .

In cases where significant outflows of emitting gas are present, as indicated by the [O III] profiles and  $\sigma_*$  measurements, the emission from non-virialized gas may contribute substantially to the narrow emission lines, particularly in their wing components. Among the narrow emission lines, the strongest outflow contributions are typically observed in [O III] (Bae et al. 2017, Kang and Woo 2018, Kovačević-Dojčinović et al. 2022), which overlaps with the broad  $\text{H}\beta$  line. In extreme cases, the [O III] outflow components exhibit complex shapes and FWHM values reaching up to  $1400 \text{ km s}^{-1}$  (see Kovačević-Dojčinović et al. 2022), making them difficult to separate from the broad  $\text{H}\beta$  profile. The inclusion of non-virialized gas emission in broad-line profiles can distort the virial "signature" on the profiles, weakening the correlation between the  $M_{\text{BH}}$  estimates from  $\text{H}\beta$  and  $\sigma_*$ . Consequently, the SMBH mass estimates based on  $\text{H}\beta$  are expected to be more reliable in objects with negligible outflow contributions.

The stronger correlation between  $\sigma_*$  and  $M_{\text{BH}}$  obtained using  $\text{H}\beta$  and  $L_{5100}$  for objects with broader  $\text{H}\beta$  profiles and higher continuum luminosity at  $\lambda 5100 \text{ \AA}$ , presents a more complex challenge to explain. Objects with broader  $\text{H}\beta$  profiles and higher luminosity generally host larger SMBHs, suggesting that  $\sigma_*$  measurements may be more uncertain for smaller SMBHs. Alternatively, narrower broad  $\text{H}\beta$  profiles may be more affected by non-virialized gas emission (see Jha et al. 2022).

Some authors address the apparent discrepancy between  $M_{\text{BH}}$  estimated for Narrow Line Seyfert 1 galaxies (NLS1s) and expectations from the host galaxy–black hole mass scaling relations, such as  $M_{\text{BH}} - \sigma_*$  (Decarli et al. 2008, 2011, Brotherton

et al. 2015). Decarli et al. (2008) propose that if BLR in NLS1s has a disc-like geometry and if these galaxies are viewed face-on, their narrow BELs result from orientation effects rather than intrinsically lower  $M_{\text{BH}}$ . This effect could lead to an underestimation of  $M_{\text{BH}}$  when using the standard methods based on  $\text{H}\beta$  for these objects, which could, in turn, result in lower correlations with  $\sigma_*$ .

Future work will aim to test the conclusions of this study on a significantly larger sample of AGN spectra, in order to confirm the obtained trends and gain a deeper understanding of their physical background. This approach could help to identify sub-samples of AGN spectra with specific BLR geometries, viewing angles, or other intrinsic physical properties, where the single-epoch  $M_{\text{BH}}$  estimators may require adjustments, such as corrections to the  $R - L$  relation or the scaling factor  $f$ .

*Acknowledgements* – The author would like to thank the anonymous referee for the valuable and thoughtful comments and suggestions, which greatly improved the clarity and quality of this manuscript. This research was supported by the Ministry of Science, Technological Development, and Innovation of the Republic of Serbia (MSTDIRS) through contract no. 451-03-136/2025-03/200 002 with Astronomical Observatory (Belgrade).

## REFERENCES

- Antonucci, R. 1993, *ARA&A*, **31**, 473
- Bae, H.-J., Woo, J.-H., Karouzos, M., et al. 2017, *ApJ*, **837**, 91
- Batiste, M., Bentz, M. C., Raimundo, S. I., Vestergaard, M. and Onken, C. A. 2017, *ApJL*, **838**, L10
- Bennert, V. N., Treu, T., Auger, M. W., et al. 2015, *ApJ*, **809**, 20
- Bentz, M. C., Peterson, B. M., Pogge, R. W., Vestergaard, M. and Onken, C. A. 2006, *ApJ*, **644**, 133
- Blandford, R. D. and McKee, C. F. 1982, *ApJ*, **255**, 419
- Bon, E., Popović, L. Č., Ilić, D. and Mediavilla, E. 2006, *NewAR*, **50**, 716
- Bon, N., Bon, E., Marziani, P. and Jovanović, P. 2015, *Ap&SS*, **360**, 7
- Brotherton, M. S., Singh, V. and Runnoe, J. 2015, *MNRAS*, **454**, 3864
- Dalla Bontà, E. and Peterson, B. M. 2022, *AN*, **343**, e210070
- Dalla Bontà, E., Peterson, B. M., Bentz, M. C., et al. 2020, *ApJ*, **903**, 112
- Dalla Bontà, E., Peterson, B. M., Grier, C. J., et al. 2025, *A&A*, **696**, 48
- Decarli, R., Dotti, M., Fontana, M. and Haardt, F. 2008, *MNRAS*, **386**, L15
- Decarli, R., Dotti, M., Haardt, F. and Zibetti, S. 2011, in *Narrow-Line Seyfert 1 Galaxies and their Place in the Universe*, ed. L. Foschini, M. Colpi, L. Gallo, D. Grupe, S. Komossa, K. Leighly, and S. Mathur, 41

- Dimitrijević, M. S., Popović, L. Č., Kovačević, J., Dačić, M. and Ilić, D. 2007, *MNRAS*, **374**, 1181
- Dojčinović, I., Kovačević-Dojčinović, J. and Popović, L. Č. 2023, *AdSpR*, **71**, 1219
- Du, P. and Wang, J.-M. 2019, *ApJ*, **886**, 42
- Ferrarese, L. and Ford, H. 2005, *SSRv*, **116**, 523
- Ferrarese, L. and Merritt, D. 2000, *ApJL*, **539**, L9
- Ferrarese, L., Pogge, R. W., Peterson, B. M., et al. 2001, *ApJL*, **555**, L79
- Gaskell, C. M. 2009, *NewAR*, **53**, 140
- Gebhardt, K., Bender, R., Bower, G., et al. 2000a, *ApJL*, **539**, L13
- Gebhardt, K., Kormendy, J., Ho, L. C., et al. 2000b, *ApJL*, **543**, L5
- Greene, J. E. and Ho, L. C. 2005, *ApJ*, **630**, 122
- Grier, C. J., Martini, P., Watson, L. C., et al. 2013, *ApJ*, **773**, 90
- Grier, C. J., Trump, J. R., Shen, Y., et al. 2017, *ApJ*, **851**, 21
- Harris, C. E., Bennert, V. N., Auger, M. W., et al. 2012, *ApJS*, **201**, 29
- Howarth, I. D. 1983, *MNRAS*, **203**, 301
- Jha, V. K., Chand, H., Ojha, V., Omar, A. and Rastogi, S. 2022, *MNRAS*, **510**, 4379
- Jonić, S., Kovačević-Dojčinović, J., Ilić, D. and Popović, L. Č. 2016, *Ap&SS*, **361**, 101
- Kang, D. and Woo, J.-H. 2018, *ApJ*, **864**, 124
- Kang, D., Woo, J.-H. and Bae, H.-J. 2017, *ApJ*, **845**, 131
- Kaspi, S., Smith, P. S., Netzer, H., et al. 2000, *ApJ*, **533**, 631
- Kaspi, S., Maoz, D., Netzer, H., et al. 2005, *ApJ*, **629**, 61
- Kovačević, J., Popović, L. Č. and Dimitrijević, M. S. 2010, *ApJS*, **189**, 15
- Kovačević-Dojčinović, J. and Popović, L. Č. 2015, *ApJS*, **221**, 35
- Kovačević-Dojčinović, J., Dojčinović, I., Lakićević, M. and Popović, L. Č. 2022, *A&A*, **659**, A130
- Kuraszkiewicz, J. K., Green, P. J., Forster, K., et al. 2002, *ApJS*, **143**, 257
- Marziani, P. 2023, *Symmetry*, **15**, 1859
- Marziani, P., Sulentic, J. W., Zwitter, T., Dultzin-Hacyan, D. and Calvani, M. 2001, *ApJ*, **558**, 553
- Mediavilla, E. and Jiménez-Vicente, J. 2021, *ApJ*, **914**, 112
- Mediavilla, E., Jiménez-Vicente, J., Fian, C., et al. 2018, *ApJ*, **862**, 104
- Mullaney, J. R., Alexander, D. M., Fine, S., et al. 2013, *MNRAS*, **433**, 622
- Netzer, H. 1977, *MNRAS*, **181**, 89
- Netzer, H. 2013, *The Physics and Evolution of Active Galactic Nuclei* (Cambridge University Press)
- Onken, C. A., Ferrarese, L., Merritt, D., et al. 2004, *ApJ*, **615**, 645
- Osterbrock, D. E. and Ferland, G. J. 2006, *Astrophysics of gaseous nebulae and active galactic nuclei* (Sausalito, CA: University Science Books)
- Peterson, B. M. 2006, in *Physics of Active Galactic Nuclei at all Scales*, ed. D. Alloin, Vol. 693, 77
- Peterson, B. M. 2014, *SSRv*, **183**, 253
- Peterson, B. M., Ferrarese, L., Gilbert, K. M., et al. 2004, *ApJ*, **613**, 682
- Popović, L. Č. 2020, *OAst*, **29**, 1
- Popović, L. Č., Vince, I., Atanacković-Vukmanović, O. and Kubičela, A. 1995, *A&A*, **293**, 309
- Popović, L. Č., Mediavilla, E., Bon, E. and Ilić, D. 2004, *A&A*, **423**, 909
- Popović, L. Č., Kovačević-Dojčinović, J. and Marčeta-Mandić, S. 2019, *MNRAS*, **484**, 3180
- Popović, L. Č., Ilić, D., Burenkov, A., et al. 2023a, *A&A*, **675**, A178
- Popović, L. Č., Kovačević-Dojčinović, J., Dojčinović, I. and Lakićević, M. 2023b, *A&A*, **679**, A34
- Punsly, B., Marziani, P., Berton, M. and Kharb, P. 2020, *ApJ*, **903**, 44
- Rakshit, S. and Woo, J.-H. 2018, *ApJ*, **865**, 5
- Schlegel, D. J., Finkbeiner, D. P. and Davis, M. 1998, *ApJ*, **500**, 525
- Sexton, R. O., Matzko, W., Darden, N., Canalizo, G. and Gorjian, V. 2021, *MNRAS*, **500**, 2871
- Shapovalova, A. I., Popović, L. Č., Burenkov, A. N., et al. 2012, *ApJS*, **202**, 10
- Shen, Y. 2013, *BASI*, **41**, 61
- Shen, Y. and Ho, L. C. 2014, *Natur*, **513**, 210
- Shen, Y., Greene, J. E., Ho, L. C., et al. 2015, *ApJ*, **805**, 96
- Sulentic, J. W., Marziani, P. and Dultzin-Hacyan, D. 2000, *ARA&A*, **38**, 521
- Thomas, D., Steele, O., Maraston, C., et al. 2013, *MNRAS*, **431**, 1383
- Tremaine, S., Gebhardt, K., Bender, R., et al. 2002, *ApJ*, **574**, 740
- Vanden Berk, D. E., Shen, J., Yip, C.-W., et al. 2006, *AJ*, **131**, 84
- Vestergaard, M. and Peterson, B. M. 2006, *ApJ*, **641**, 689
- Vietri, G., Piconcelli, E., Bischetti, M., et al. 2018, *A&A*, **617**, A81
- Woo, J.-H., Yoon, Y., Park, S., Park, D. and Kim, S. C. 2015, *ApJ*, **801**, 38
- Woo, J.-H., Bae, H.-J., Son, D. and Karouzos, M. 2016, *ApJ*, **817**, 108
- Woo, J.-H., Son, D. and Rakshit, S. 2020, *ApJ*, **901**, 66
- Yip, C., Connolly, A., vanden Berk, D., et al. 2004a, in *Astronomical Society of the Pacific Conference Series*, Vol. 311, *AGN Physics with the Sloan Digital Sky Survey*, ed. G. T. Richards and P. B. Hall, 17
- Yip, C. W., Connolly, A. J., Szalay, A. S., et al. 2004b, *AJ*, **128**, 585
- Yip, C. W., Connolly, A. J., Vanden Berk, D. E., et al. 2004c, *AJ*, **128**, 2603
- Zamanov, R., Marziani, P., Sulentic, J. W., et al. 2002, *ApJL*, **576**, L9
- Zheng, W. and Sulentic, J. W. 1990, *ApJ*, **350**, 512

ПОУЗДАНОСТ ПРОЦЕНЕ МАСА ЦРНИХ РУПА У АКТИВНИМ ГАЛАКТИЧКИМ  
ЈЕЗГРИМА ТИПА 1 КОРИШЋЕЊЕМ ШИРОКИХ ЕМИСИОНИХ ЛИНИЈА

Слађана Марчета-Мандић<sup>1,2</sup> 

<sup>1</sup>Астрономска опсерваторија, Волгина 7, 11060 Београд 38, Србија

<sup>2</sup>Катедра за астрономију, Математички факултет, Универзитет у Београду  
Студентски трг 16, 11000 Београд, Србија

E-mail: [sladjana@aob.rs](mailto:sladjana@aob.rs)

УДК 523.342 : 523.342.6 : 523.985 : 535.5

Оригинални научни рад

У овом раду представљено је истраживање поузданости процене маса црних рупа ( $M_{\text{BH}}$ ) коришћењем широких емисионих линија из спектра активних галактичких језгара (AGN) типа 1, преузетих из Sloan Digital Sky Survey (SDSS) базе. Масе црних рупа добијене из широких емисионих линија  $\text{H}\alpha$  и  $\text{H}\beta$  упоређене су са дисперзијом брзина звезда ( $\sigma_*$ ) из галактичког овала (*bulge*) активних галаксија. Резултати показују да се корелација  $M_{\text{BH}}-\sigma_*$  по-

бољшава у оним подзорцима које карактеришу следеће спектралне особине: шира широка  $\text{H}\beta$  линија, црвена асиметрија у  $\text{H}\beta$  профилима емисионих линија, висока луминозност континуума и одсуство избацивања материје из активног језгра (*outflows*). Ови резултати указују на то да  $\text{H}\alpha$  и  $\text{H}\beta$  пружају прецизније процене масе црне рупе за објекте са наведеним спектралним карактеристикама.